Engineering with Computers
https://doi.org/10.1007/s00366-023-01906-8

ORIGINAL ARTICLE

Multiscale modeling of functionally graded shell lattice metamaterials for additive manufacturing

M. Shojaee[1] · I. Valizadeh[1] · D. K. Klein[1] · P. Sharifi[2] · O. Weeger[1]

Received: 4 May 2023 / Accepted: 17 September 2023

Abstract
In this work, an experimentally validated multiscale modeling framework for additively manufactured shell lattice structures with graded parameters is introduced. It is exemplified in application to the Schwarz primitive triply periodic minimal surface microstructure and 3D printing using masked stereolithography of a photopolymer material. The systematic procedure starts with the characterization of a hyperelastic material model for the 3D printed material. This constitutive model is then employed in the finite element simulation of shell lattices at finite deformations. The computational model is validated with experimental compression tests of printed lattice structures. In this way, the numerical convergence behavior and size dependence of the model are assessed, and the range in which it is reasonable to assume linear elastic behavior is determined. Then, representative volume elements subject to periodic boundary conditions are simulated to homogenize the mechanical behavior of Schwarz primitives with varying aspect ratios and shell thicknesses. Subsequently, the parameterized effective linear elasticity tensor of the metamaterial is represented by a physics-augmented neural network model. With this constitutive model, functionally graded shell lattice structures with varying microstructural parameters are simulated as macroscale continua using finite element and differential quadrature methods. The accuracy, reliability and effectiveness of this multiscale simulation approach are investigated and discussed. Overall, it is shown that this experimentally validated multiscale simulation framework, which is likewise applicable to other shell-like metamaterials, facilitates the design of functionally graded structures through additive manufacturing.

Keywords Metamaterials · Functionally graded materials · Multiscale modeling · Physics-augmented machine learning · Additive manufacturing

1 Introduction

Additive manufacturing (AM) has in particular enabled the fabrication of lattice structures composed of repeating patterns of metamaterials with beam, plate, thin-walled, shell-like, or multi-phase solid geometries. The mechanical behavior of a metamaterial is determined by the base materials it is made of, as well as the topology and geometrical parameters of the (periodically) repeated unit cell (RUC). In particular, metamaterials with slender, beam- or shell-like microstructures offer a unique combination of lightweight, high strength, and efficient load distribution [1–3]. Furthermore, AM allows to functionally grade (FG) structures by varying the microstructure, e.g., by locally adjusting material, topological, or design geometrical parameters [4, 5]. For instance, Choy et al. [6] conducted an experimental study and found that FG beam lattices exhibit higher plateau stress and specific energy absorption compared to homogeneous lattices. Bai et al. [7] performed an experimental and numerical study on size-graded beam lattice structures with varying topological parameters. Alternatively, graded lattices can be created in additive manufacturing by gradually adjusting material properties, e.g., by mixing constituents [8] or adjusting the degree of polymerization [9, 10]. To explore this technique, Kim et al. [11] carried out an experimental study to improve surface hardness and flexural stiffness of FG beam lattices

✉ M. Shojaee
shojaee@cps.tu-darmstadt.de

[1] Cyber-Physical Simulation Group, Department of Mechanical Engineering, Technical University of Darmstadt, Dolivostr. 15, Darmstadt 64293, Hessen, Germany

[2] School of Mechanical Engineering, Shiraz University, Shiraz 71936-16548, Fars, Iran

Published online: 11 October 2023

using varying degrees of polymerization. Furthermore, a non-periodic class of functionally graded spinodoid topologies was introduced in [12].

In particular, RUCs consisting of shell-like microstructures such as triply periodic minimal surfaces (TPMS) have been shown to ideally combine high structural strength with low effective density, which makes them suitable for the efficient design of lightweight structures [13]. Triply periodic minimal surfaces are usually defined by implicit equations and repeat periodically in three dimensions with a certain material symmetry [14]. TPMS lattice structures fabricated by selective laser melting are of interest in a variety of fields due to their unique geometric and mechanical properties, including their minimal surface area and their ability to resist compressive loads [15]. An extensive investigation of the mechanical performance of additively manufactured shell-lattice metamaterials using simulations and experiments was carried out in [16]. Guo et al. [17] proposed different shapes and opening diameters for uniform lattice structures consisting of the Schwarz primitive (SP), a common TPMS, to enhance its mechanical properties and energy absorption. The implementation of FG TPMS lattice structures in engineering applications has been boosted in recent years due to the advancement of AM technologies, which have eliminated many constraints on the realization of geometrically intricate and graded microstructures [18]. In this regard, Plocher and Panesar [19] reported on an experimental investigation of the effect of density and topology grading on the stiffness and energy absorption of additively manufactured FG TPMS lattices with a small number of unit cells. They confirmed that the severity of density grading had a positive effect on the total compressive stiffness of the SP TPMS. Similarly, in [20] the effect of varying unit cell size on the energy absorption behaviour of additively manufactured TPMS structures was experimentally studied. Furthermore, in [21] the shape memory effect of TPMS lattice structures made from polymers was investigated. However, the mechanical behavior of FG TPMS lattices has not been intensively investigated yet and in particular, no approaches have been proposed yet that would facilitate the computational design of FG lattices with a large number of TPMS RUCs.

Since structures composed of thousands or even millions of RUCs of a metamaterial can hardly be computationally modeled at full-scale, multiscale modeling techniques must be applied [22]. In a number of works, the numerical homogenization method has been used to determine the elastic moduli of uniform TPMS structures, including dependencies on the effective density of the RUCs [16, 23–26]. Recently, these microstructural characterizations were also carried out for as-manufactured TPMS geometries obtained from imaging data and including manufacturing imperfections [27, 28]. Furthermore, Jian et al. [29] proposed a numerical approach using multiscale mechanical topology optimization to improve the compressive properties of FG TPMS. The properties of the optimized designs were improved over a uniform structure by almost 25%. Even though multiscale analysis methods have been applied to TPMS lattices, none of the mentioned works verifies their (microstructural) simulation approach in application to a concrete AM technique and connects the homogenization to a sequential multiscale simulation. Furthermore, material models that include dependencies on geometric parameters of the TPMS microstructures have not been derived yet.

In this regard, the adoption of machine learning techniques provides many opportunities for multiscale modeling [30]. In particular for representing constitutive relations, many approaches have been presented in recent years that employ artificial, feed-forward neural networks (ANNs, FFNNs) [31, 32] due to their flexibility and universal approximation capabilities [33]. For instance, an FFNN architecture that allows to preserve the symmetric positive definiteness of linear elastic constitutive tensors was presented in [34] and then also applied in [35]. The flexibility of ANNs has also been largely exploited to formulate nonlinear, hyperelastic, inelastic, and multiphysical material models [36–42]. However, to ensure the physical sensibility and generalizability of a material model, ANNs should as much as possible be augmented with physical requirements [43], i.e., they should fulfill by construction properties such as thermodynamic consistency [37, 41] or convexity requirements [34, 36]. In the context of linear elasticity, microstructural dependencies of the homogenized elasticity tensors in the form of image data have been considered in [44, 45] using deep convolutional neural networks. Furthermore, also hyperelastic FFNN models have already been enhanced with parametric dependencies, e.g., of homogenized beam lattice metamaterials [46], and were used in multiscale simulations [47]. Generally, both hyperelastic constitutive models as well as parameterized linear elasticity tensors are multi-dimensional, nonlinear functions, which are difficult to represent. Thus, neural networks are highly suitable candidates for formulating such models.

This manuscript aims to introduce a systematic multiscale modeling technique for additively manufactured, functionally graded TPMS lattices. For its demonstration, the multiscale modeling framework is applied to the parameterized Schwarz primitive TPMS and realized by masked stereolithography (MSLA) 3D printing. Besides the full-scale simulation and microscale homogenization using shell finite elements, one of the key ingredients of the proposed approach is the use of a physics-augmented FFNN to accurately predict the effective elasticity tensor of the SP TPMS, which incorporates the dependency on four geometrical parameters.

The further structure of this manuscript is as follows. In Sect. 2, the methodologies applied in this work are described, including the geometric modeling of the Schwarz primitive, the computational modeling of lattices at full-scale, microscale, and macroscale, the homogenization and parameterized effective constitutive modeling with neural networks, and the experimental setup using MSLA 3D printing. Then, in Sect. 3 the results are presented from the experimental validation of the simulation model, to the investigation of the microscale behavior of the SP, to the homogenized, effective material modeling, and to the multiscale simulation and its verification. Finally, the manuscript concludes with a summary and outlook in Sect. 4.

2 Methods

Since the fully resolved design and simulation of additively manufactured structures comprised of metamaterials with thousands of unit cells such as TPMS is computationally challenging and inefficient, our aim is to establish a multiscale simulation framework. The main methodological ingredients and steps in this approach, which are also illustrated in Fig. 1 are:

1. The parameterized geometric design of the unit cell of the metamaterial, here the Schwarz primitive TPMS (Sect. 2.1).
2. The computation modeling of the mechanical behavior of the shell lattice structures and unit cells (Sect. 2.2) for which an experimentally characterized constitutive model of the 3D printed material is required and which has to be experimentally validated (Sect. 2.5).
3. The numerical homogenization of the effective mechanical behavior of the unit cells (Sect. 2.3) and the determination of a parameterized effective material model (Sect. 2.4) that allows to represent functionally graded structures in macroscopic simulations (Sect. 2.2).

As mentioned, we demonstrate and validate this framework here in application to the Schwarz primitive TPMS fabricated by MSLA 3D printing, but it could likewise be applied to other shell lattice metamaterials and additive manufacturing methods.

2.1 Geometric model of parameterized Schwarz primitive

The Schwarz primitive (SP) is a common TPMS. The mid-surface of a Schwarz primitive RUC is defined using a local coordinate system $(\bar{x}, \bar{y}, \bar{z}) \in [-a, a] \times [-b, b] \times [-c, c]$ and can be expressed using the following implicit equation:

$$\cos\frac{\pi\bar{x}}{a} + \cos\frac{\pi\bar{y}}{b} + \cos\frac{\pi\bar{z}}{c} = const. \tag{1}$$

The geometrical parameters a, b, c control the length, width, and height of the RUC of the SP, which is depicted in Fig. 2. Here, we model the RUCs in the computer-aided design software Siemens NX, where the constant in Eq. (1) is chosen in such a way that the cross sections of the unit cell have an elliptical profile. For numerical simulation, see Sect. 2.2, the surface geometry can be exported in STEP file format and meshed using shell finite elements. For 3D printing, see Sect. 2.5, the surfaces defined by Eq.

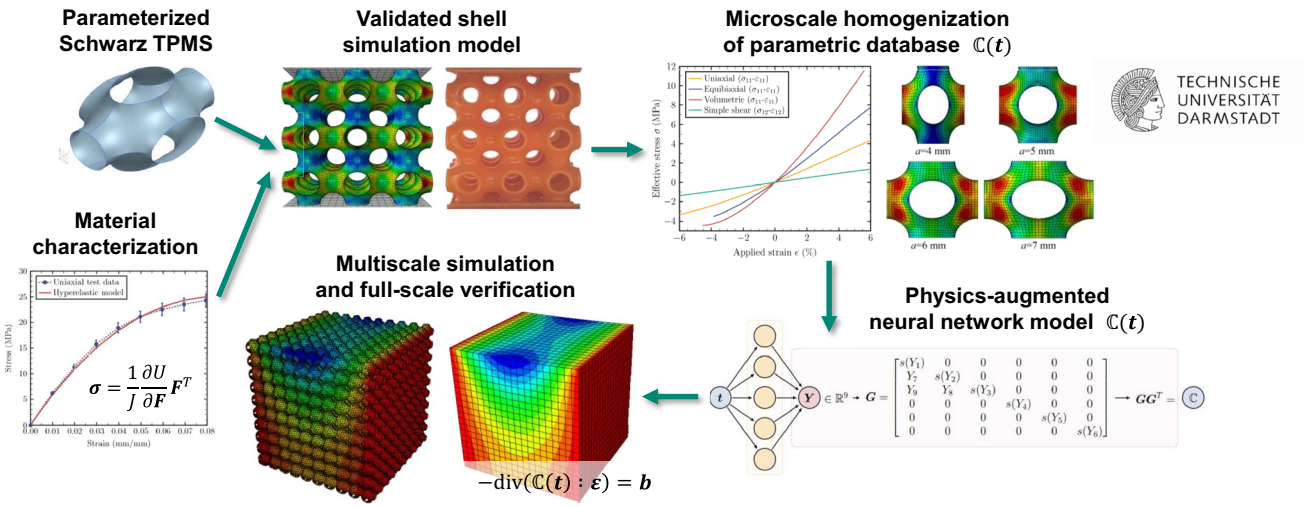

Fig. 1 Illustration of the proposed multiscale simulation workflow

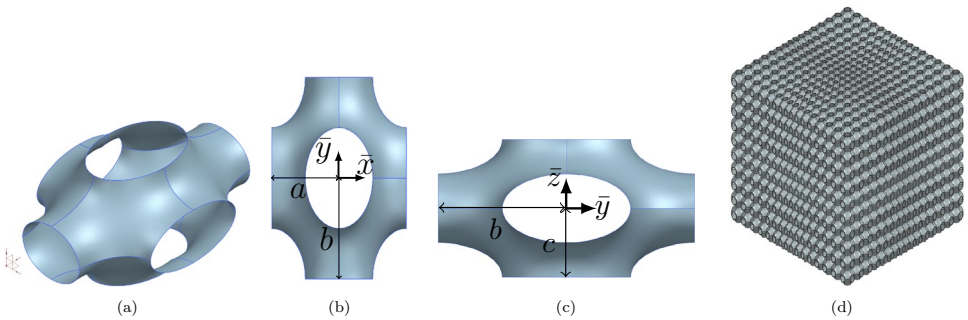

Fig. 2 Geometric modeling of the Schwarz primitive TPMS. **a**–**c** show 3D and 2D views of the mid-plane geometry of the SP RUC, with the 2D views highlighting the geometrical parameters of the unit cell. **c** Illustrates a functionally graded structure made of non-uniform SP RUCs with varying parameters

(1) are extruded by $\pm h/2$ in the normal direction, which yields a shell-like, volumetric structure of thickness h that can be exported in STL file format. Overall, the geometric dimensions, and thus also the mechanical behavior, of SP shell lattice RUCs are controlled by the parameters $\boldsymbol{t} = (a, b, c, h)$.

2.2 Shell model for direct and microscale simulation

Slender structures such as TPMS and in particular the SP can be mechanically modelled using shell theories, in which only the displacements (and rotations) of the mid-surface are considered as independent degrees of freedom. Here, we employ the finite strain shell formulation based on 4-node finite elements with bilinear interpolation of displacements and rotation updates, using reduced integration with hourglass control, as implemented in the "S4R" element in the Abaqus CAE software [48]. The quadrilateral finite element meshes, see e.g. Fig. 6, are also generated in Abaqus from the geometries imported in STEP file format. Special attention is put on creating meshes with nodes aligned at corresponding positions on opposite edges, as this is favorable for homogenization, see Sect. 2.3.

Within the finite strain shell theory, hyperelastic material behavior is assumed. Here, the near incompressible Mooney-Rivlin constitutive model, which is widely used in the analysis of polymers, is adopted. The Cauchy stress tensor $\boldsymbol{\sigma}$ can be computed from the strain energy function U of the Mooney-Rivlin model as:

$$\begin{aligned}\boldsymbol{\sigma} &= \frac{1}{J}\frac{\partial U}{\partial \boldsymbol{F}}\boldsymbol{F}^T \quad \text{with} \quad U(\boldsymbol{F}) \\ &\equiv U(\bar{I}_1, \bar{I}_2, J) = D_{10}(\bar{I}_1 - 3) + D_{01}(\bar{I}_2 - 3) + \frac{1}{D_2}(J-1)^2,\end{aligned} \tag{2}$$

where $J = \det(\boldsymbol{F})$ is the determinant of the deformation gradient tensor $\boldsymbol{F}$ and $\bar{I}_1 = J^{-2/3} I_1$, $\bar{I}_2 = J^{-4/3} I_2$ are the isochoric invariants, which can be computed using J and the first and second invariants of the right Cauchy-Green strain tensor $\boldsymbol{C} = \boldsymbol{F}^T\boldsymbol{F}$: $I_1 = \mathrm{tr}(\boldsymbol{C})$, $I_2 = (\mathrm{tr}(\boldsymbol{C})^2 - \mathrm{tr}(\boldsymbol{C}^2))/2$ [49]. The specific material behavior is defined by the three material parameters D_{10}, D_{01}, and D_2, which are to be determined experimentally.

Since the numerical modeling using a shell formulation is computationally much more efficient than using the 3D continuum elements, not only (microscopic) RUCs of the SP, but also (macroscopic) structures consisting of a moderate amount of unit cells can be directly simulated on desktop computers in a reasonable amount of time. The direct simulations serve for the experimental validation of the simulation model, while the microscale simulations are the basis of the multiscale simulation, see Sect. 2.3.

2.3 Multiscale simulation and homogenization

Mechanical multiscale simulations are based on the concept of scale separation and the Hill-Mandel principle, which state that the virtual work at any point in a macroscopic continuum is equal to the volume average of the virtual work of a representative volume element (RVE) of the microstructure, if the microstructure is periodically repeated and infinitesimally small compared to the macro continuum [50]. The RVE should be large enough to include all the relevant microstructural features and characteristic behaviors, and can thus also consist of multiple periodic RUCs, but small enough to be considered as a point in the macroscale [51]. For instance, in Fig. 2, (d) would refer to the macro structure that could be regarded as a continuum, since it consists of many periodically repeated cells, which are shown in (a).

As will be investigated in Sect. 3.2, the effective behavior of SP TPMS can be well approximated as linear elastic within a strain range of -2% to 4%. For higher compressive strains instabilities may occur that restrict multiscale approaches and for larger tensile strains the material may already exhibit plastic deformations. Thus, for the multiscale modeling of the SP TPMS, we restrict ourselves here to linear elasticity. Then, the Hill-Mandel condition can be formulated as:

$$\delta\boldsymbol{\varepsilon} : \boldsymbol{\sigma} = \langle \delta\boldsymbol{\varepsilon}_m \rangle : \langle \boldsymbol{\sigma}_m \rangle = \langle \delta\boldsymbol{\varepsilon}_m : \boldsymbol{\sigma}_m \rangle, \tag{3}$$

where $\boldsymbol{\varepsilon}$ and $\boldsymbol{\sigma}$ stand for the linear strain and Cauchy stress tensors at the macro scale, the subscript m indicates their microscale counterparts, and $\langle\cdot\rangle$ symbolizes the volume

average over the microscale RVE [50]. Since in linear elasticity the macroscopic stress tensor can be expressed as $\boldsymbol{\sigma} = \mathbb{C} : \boldsymbol{\varepsilon}$, the aim is to determine a corresponding fourth-order elasticity tensor $\mathbb{C}$ that captures the effective, averaged behavior of the microscale.

Generally, the fulfillment of the Hill-Mandel condition Eq. (3) can be ensured by applying macroscale strains or stresses to the RVE using suitable boundary conditions. Typically, periodic boundary conditions are employed, which ensure compatible deformations and tractions at opposing faces of the RVE. To fully determine the effective constitutive tensor $\mathbb{C}$, it is then only necessary to carry out 6 homogenizations of the RVE, in each of which either a uniaxial strain state with only $\varepsilon_{11} = \epsilon \neq 0$, or only $\varepsilon_{22} = \epsilon$, or only $\varepsilon_{33} = \epsilon$, or a simple shear deformation state with only $\varepsilon_{23} = \epsilon \neq 0$, or only $\varepsilon_{13} = \epsilon$, or only $\varepsilon_{12} = \epsilon$ is prescribed, respectively (with ϵ specifying the applied strain). From the resulting stress tensors $\boldsymbol{\sigma} = \langle \boldsymbol{\sigma}_m \rangle$, all 21 independent components C_{ijkl} can be computed. Since the dimensions a, b, and c of the RUCs can have different values, the parameterized SP possess a rhombic material symmetry, which allows to represent the constitutive model in Voigt notation as:

$$\boldsymbol{\sigma} = \mathbb{C}{:}\boldsymbol{\varepsilon} \quad \Leftrightarrow \quad \begin{bmatrix} \sigma_{11} \\ \sigma_{22} \\ \sigma_{33} \\ \sigma_{23} \\ \sigma_{31} \\ \sigma_{12} \end{bmatrix} = \begin{bmatrix} C_{1111} & C_{1122} & C_{1133} & 0 & 0 & 0 \\ C_{1122} & C_{2222} & C_{2233} & 0 & 0 & 0 \\ C_{1133} & C_{2233} & C_{3333} & 0 & 0 & 0 \\ 0 & 0 & 0 & C_{2323} & 0 & 0 \\ 0 & 0 & 0 & 0 & C_{3131} & 0 \\ 0 & 0 & 0 & 0 & 0 & C_{1212} \end{bmatrix} \begin{bmatrix} \varepsilon_{11} \\ \varepsilon_{22} \\ \varepsilon_{33} \\ 2\varepsilon_{23} \\ 2\varepsilon_{31} \\ 2\varepsilon_{12} \end{bmatrix}, \tag{4}$$

with only 9 independent, non-zero coefficients, see [52, Sec. 3.4] and [53, Sec. 9.3.2].

Ultimately, a multiscale simulation of a structure consisting of many periodically repeated TPMS unit cells can simply be carried out as a simulation of the macroscale 3D continuum. Thus, the linear elasticity equation:

$$-\operatorname{div}\left(\mathbb{C}(\boldsymbol{t}) : \boldsymbol{\varepsilon}\right) = \boldsymbol{b} \tag{5}$$

together with appropriate boundary conditions, needs to be solved, in which the constitutive model defined by the homogenized (parameter-dependent) $\mathbb{C}(\boldsymbol{t})$ is used. Here, we perform such multiscale or macroscale simulations in two ways, using a finite element discretization in Abaqus [48], or using a differential quadrature method (DQM) [54, 55].

While it is difficult to consider three-dimensionally graded microstructures with location-dependent material behavior $\mathbb{C}(\boldsymbol{t}) \equiv \mathbb{C}(\boldsymbol{x})$ in commercial FEA software such as Abaqus, this is easier to realize in an in-house DQM program. For instance, in [56] one-dimensional functional grading was realized by a user material routine (UMAT) in Abaqus. Based on the three-dimensional constitutive relations and the strain–displacement relations, the governing differential equations of Eq. (5) can be written as:

$$\frac{\partial}{\partial x_j}\left[\frac{C_{ijkl}(x_1, x_2, x_3)}{2}\left(\frac{\partial u_k}{\partial x_l} + \frac{\partial u_l}{\partial x_k}\right)\right] = b_i \text{ for } i = 1, 2, 3. \tag{6}$$

Using the DQM, these partial differential equation are discretized on a given grid $(x_1^m, x_2^n, x_3^s) = \boldsymbol{x}^{mns}$ with $m = 1, \ldots, N_x$, $n = 1, \ldots, N_y$, $s = 1, \ldots, N_z$ as:

$$\left.\frac{\partial u_k}{\partial x_l}\right|_{\boldsymbol{x}^{mns}} = \sum_{p,q,r=1}^{N_x,N_y,N_z} A_l^{mnspqr} u_k^{pqr}, \qquad \left.\frac{\partial u_k}{\partial x_l \partial x_g}\right|_{\boldsymbol{x}^{mns}} = \sum_{p,q,r=1}^{N_x,N_y,N_z} B_{lg}^{mnspqr} u_k^{pqr}, \tag{7}$$

where N_x, N_y, N_z are the number of grid points along the direction of x_1, x_2, x_3, respectively, and A_l^{mnspqr} and B_{lg}^{mnspqr} denote the weighting coefficients of first-order and second-order derivatives, respectively, see [54, 55] for details. Finally, by applying the differential quadrature rules, a system of algebraic equations is obtained, which can be solved for the displacement coefficients of the grid points u_k^{pqr}.

2.4 Parameterized material modeling with neural networks

Above, the homogenization of the effective constitutive tensor $\mathbb{C}$ for a given microstructure has been described. However, here we want to facilitate the multiscale simulation of functionally graded shell lattices with arbitrarily (within a certain range) varying geometric design parameters of the SP RUC, see Sect. 2.1. This would entail that a numerical homogenization procedure according to Sect. 2.3 has to be carried out for each quadrature point within a macroscale FEM or DQM with the microstructural parameters given at that point. To avoid this high computational effort, we introduce a parameterized material model, which is to be realized through a physics-augmented neural network.

As mentioned above, the linear elastic material model for the parameterized SP is defined through the 9 independent coefficients of $\mathbb{C}$, see Eq. (4). However, to yield only positive energy densities:

$$U(\boldsymbol{\varepsilon}) = \tfrac{1}{2}\,\boldsymbol{\varepsilon} : \mathbb{C} : \boldsymbol{\varepsilon} \geq 0 \quad \forall \boldsymbol{\varepsilon}, \tag{8}$$

the elasticity tensor has to be positive semi-definite. This applies in both the fourth-order tensor and the Voigt notations. Thus, positive semi-definiteness can be ensured by expressing $\mathbb{C} \in \mathbb{R}^{6\times6}$ by its the Cholesky decomposition $\mathbb{C} = \boldsymbol{G}\boldsymbol{G}^T$, see [57, Corollary 7.2.9], where $\boldsymbol{G} \in \mathbb{R}^{6\times6}$ is a lower triangular matrix with non-negative diagonal entries. For the rhombic material symmetry group, the Cholesky matrix $\boldsymbol{G}$ can be restricted to the form:

$$\boldsymbol{G} = \begin{bmatrix} G_{11} & 0 & 0 & 0 & 0 & 0 \\ G_{21} & G_{22} & 0 & 0 & 0 & 0 \\ G_{31} & G_{32} & G_{33} & 0 & 0 & 0 \\ 0 & 0 & 0 & G_{44} & 0 & 0 \\ 0 & 0 & 0 & 0 & G_{55} & 0 \\ 0 & 0 & 0 & 0 & 0 & G_{66} \end{bmatrix}, \tag{9}$$

which leads to:

$$\begin{aligned} \mathbb{C} &= \boldsymbol{G}\boldsymbol{G}^T \\ &= \begin{bmatrix} G_{11}^2 & G_{11}G_{21} & G_{11}G_{31} & 0 & 0 & 0 \\ G_{11}G_{21} & G_{21}^2 + G_{22}^2 & G_{21}G_{31} + G_{22}G_{32} & 0 & 0 & 0 \\ G_{11}G_{31} & G_{21}G_{31} + G_{22}G_{32} & G_{31}^2 + G_{32}^2 + G_{33}^2 & 0 & 0 & 0 \\ 0 & 0 & 0 & G_{44}^2 & 0 & 0 \\ 0 & 0 & 0 & 0 & G_{55}^2 & 0 \\ 0 & 0 & 0 & 0 & 0 & G_{66}^2 \end{bmatrix}. \end{aligned} \tag{10}$$

Thus, we may represent the rhombic elasticity tensor $\mathbb{C}$ in terms of the 9 components of $\boldsymbol{G}$, which then automatically fulfills the condition of positive semi-definiteness as well as the restrictions on the specific components.

As mentioned, for functionally graded bodies, the macroscopic elasticity tensor is not a constant but depends on microstructural parameters, e.g., the geometrical parameters of the Schwarz RUC, here a, b, c, and h, see Sect. 2.1. We summarize these four parameters in a vector $\boldsymbol{t} = (a, b, c, h)$ and express the parametric dependency of the elasticity tensor through its Cholesky matrix:

$$\mathbb{C}(\boldsymbol{t}) = \boldsymbol{G}(\boldsymbol{t})\, \boldsymbol{G}(\boldsymbol{t})^T, \tag{11}$$

Finding an explicit form for $\boldsymbol{G}(\boldsymbol{t})$, or rather of its 9 independent coefficients, see Eq. (9), is not straightforward, as the functional relationship may be arbitrary nonlinear and complex, depending on the microstructure under consideration, in particular with an increasing amount of geometrical parameters. Thus, we want to apply FFNNs [31, 32], which can represent arbitrary complex functional relationships [33]. By representing $\boldsymbol{G}(\boldsymbol{t})$ with a FFNN, we can exploit their extraordinary flexibility, while at the same time, all physical properties of $\mathbb{C}$ are preserved, i.e., the neural network model used to represent $\mathbb{C}(\boldsymbol{t})$ is "augmented" with the physical requirements of positive definiteness and material symmetry, compare also [34].

In this work, FFNNs with a single hidden layer with 32 nodes and a linear output layer are employed to map the input vector $\boldsymbol{t} = (a, b, c, h) \in \mathbb{R}^4$ to the output vector $\boldsymbol{y} \in \mathbb{R}^9$ as:

$$\boldsymbol{y} = \boldsymbol{W}^2\, s\left(\boldsymbol{W}^1\boldsymbol{t} + \boldsymbol{b}^1\right) + \boldsymbol{b}^2. \tag{12}$$

Here, $\boldsymbol{W}^1 \in \mathbb{R}^{32\times4}$, $\boldsymbol{W}^2 \in \mathbb{R}^{9\times32}$ are weight matrices, $\boldsymbol{b}^1 \in \mathbb{R}^{32}$, $\boldsymbol{b}^2 \in \mathbb{R}^9$ bias vectors, and $s(x) = \log(1 + \exp(x))$ symbolizes the softplus activation function, which acts on vectors component-wise.

Since the 6 diagonal coefficients of $\boldsymbol{G}$ must be positive, they are obtained from the first 6 outputs by again applying the softplus function, while the remaining 3 coefficients are directly related to the remaining 3 outputs:

$$G_{ii} = s(y_i), \quad i = 1, \dots, 6, \qquad G_{21} = y_7, \quad G_{32} = y_8, \quad G_{31} = y_9. \tag{13}$$

In Fig. 3, the overall structure and flow of this physics-augmented neural network model are illustrated.

To train the FFNN, i.e., to determine its so-called hyperparameters $\{\boldsymbol{W}^1, \boldsymbol{W}^2, \boldsymbol{b}^1, \boldsymbol{b}^2\}$ such that it yields an

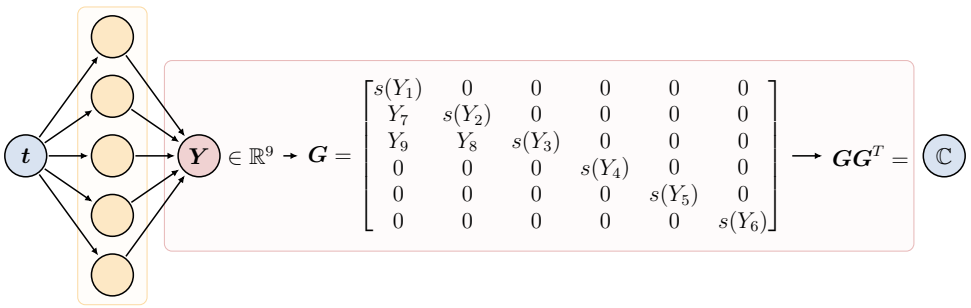

Fig. 3 Illustration of the physics-augmented neural network architecture used to represent the parameterized effective constitutive model of the Schwarz primitive. The geometrical parameters $\boldsymbol{t} = (a, b, c, h)$ of the RUC serve as inputs to the single-layered FFNN (yellow color). The p.s.d. rhombic structural tensor $\mathbb{C}(\boldsymbol{t})$ is calculated through its Cholesky matrix $\boldsymbol{G}(\boldsymbol{t})$, where the softplus function s ensures positivity of the diagonal components

approximation of the functional relationship $\boldsymbol{G}(\boldsymbol{t})$, a dataset of the form

$$\mathcal{D} = \left\{ \left(\boldsymbol{t}_1, \hat{\mathbb{C}}_1 \right), \dots \left(\boldsymbol{t}_n, \hat{\mathbb{C}}_n \right) \right\}, \tag{14}$$

is obtained from the homogenization of the linear elasticity tensors, see Sect. 2.3, which consists of tuples of geometrical parameters $\boldsymbol{t}_i$ and corresponding effective elasticity tensors $\hat{\mathbb{C}}_i$. Then, a nonlinear optimization algorithm, here the Adam optimizer with a learning rate of 0.002 and 5000 iterations, is applied to minimize the mean squared error of the deviations of the homogenized elasticity tensors from the ones predicted by the physics-augmented NN:

$$\text{MSE} := \frac{1}{n} \sum_{i=1}^{n} \| \hat{\mathbb{C}}_i - \mathbb{C}(\boldsymbol{t}_i) \|^2. \tag{15}$$

Note that for the application here, the single-layered FFNN architecture from Eq. (12) has been shown to be sufficiently flexible to represent the dependency of the elasticity tensor of the SP TPMS on its 4 geometric parameters. Similar observations have also been made for hyperelastic constitutive models, cf. [37, 38, 58]. However, the approach presented in this work does not depend on the activation function or number of hidden layers of the FFNN, and thus may be also applied for multilayered network architectures and other activation functions.

2.5 Experimental setup

Here, the manufacturing and mechanical characterization of SP TPMS structures is exemplary and carried out using MSLA 3D printing of a photo-curable polymer material. The specimens are fabricated using the commercial MSLA 3D printer "Original Prusa SL1S" by Prusa Research a.s. This printer is equipped with a monochrome LCD module, a UV LED with 405 nm wavelength, and the maximum irradiance is ca. 3.6 mW/cm^2. The display has a size of 120 mm × 68 mm and a resolution of 2560 × 1620 pixels. The specimens are produced using the UV-sensitive "Prusament Resin Tough Prusa Orange", a material also developed by Prusa Research a.s. The composition of the material includes epoxy resin (20% – 40%), color pigment (2% – 5%), and photoinitiators (3% – 5%). The specimens are printed with a layer thickness of 0.05 mm, an initial exposure time of 10 s for the first 10 layers, and an exposure time of 3 s for all remaining layers.

To characterize the mechanical properties of the material, uniaxial tension tests are performed according to the ASTM D638 standard. The geometries of the 3D-printed samples are chosen according to sample type IV. A T500-1200-5kN machine (MFC Sensortechnik GmbH) is utilized for the tests, in accordance with EN ISO 7500-1 standard. The machine has a travel resolution accuracy of 1 μm. Furthermore, to evaluate the mechanical behavior of Schwarz P lattices, samples with 3×3×3 RUCs are fabricated with various shell thickness $h = 0.4, 0.6, 0.8, 1.0, 1.2, 1.4$ mm and the shell geometry parameters are $a = b = c = 5$ mm, compare Fig. 2. These structures are subjected to compression testing with a crosshead speed of 5 mm/min, i.e., a quasi-static strain rate of ca. 0.0028 1/s.

3 Results

3.1 Experimental validation of the simulation model

The numerical homogenization of the effective mechanical behavior of an RVE requires a validated simulation model. Thus, the first step is the experimental characterization of the hyperelastic material model of the 3D-printed polymer. As outlined in Sect. 2.5, for this purpose tensile tests are carried out on MSLA printed standard samples. Then, the three parameters of the hyperelastic Mooney-Rivlin material model given in Eq. (2) are fitted to approximate the stress–strain relation. Here, the coefficients of the Mooney-Rivlin model from Eq. (2) are obtained as $D_{10} = -564.35$ MPa, $D_{01} = 670.22$ MPa, $D_2 = 0.00157$ MPa^{-1}. Figure 4 shows the stress–strain

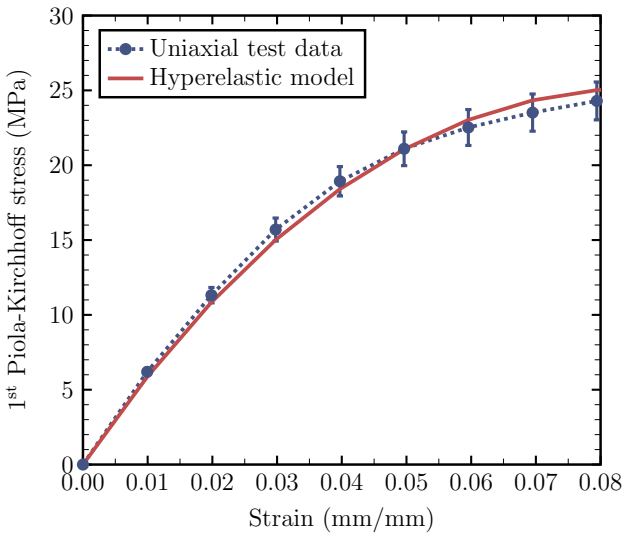

Fig. 4 Comparison of experimental stress–strain curves with fitted hyperelastic material model for a uniaxial tension test of the MSLA 3D printed material

curves for both the experimental uniaxial tension tests, as well as the fitted Mooney-Rivlin model.

This material model and parameters are then used in direct simulations of Schwarz primitive lattice structures, which consist of 3×3×3 RUCs with geometry parameters $a = b = c = 5$ mm and shell thickness $h = 0.4$ mm, i.e., the aspect ratio is $h/a = 0.08$ and the overall size of the structure is 30×30×30 mm. First, a convergence study is carried out to assess the accuracy of the FEM using finite strain shell elements. For this purpose S4R meshes with increasing numbers of elements (from 208 to 784, to 1792, and to 3236 elements per RUC) are generated and simulated. The relationship between the applied compressive displacement and the resulting compressive force is plotted for these four meshes in Fig. 5. First of all, it can be seen that the shell finite element discretization converges with mesh refinement. Since the results for 1792 and 3236 elements per RUC are hardly distinguishable, we proceed in all subsequent FE calculations with 1792 elements.

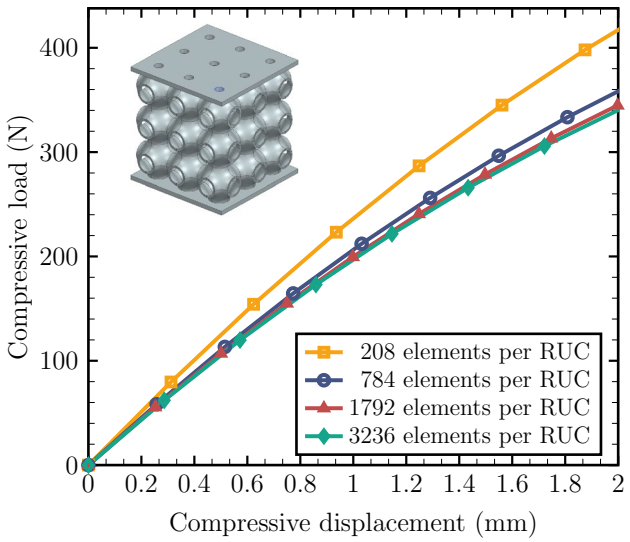

Fig. 5 Convergence study of the simulation results with different numbers of elements for the compression test of a lattice structure with $3 \times 3 \times 3$ Schwarz primitve RUCs with $a = b = c = 5$ mm and $h = 0.4$ mm

Furthermore, in Fig. 5 it can be observed that the lattice structure becomes increasingly nonlinear as the compressive displacement increases up to 2 mm (i.e., 6.67% strain of the structure). This behavior is commonly observed in lattice structures and metamaterials and can be mostly attributed to geometrically nonlinear effects that stem from the bending of the shell. The analysis of this nonlinear behavior is crucial for estimating the range of applied structural strain, in which it is acceptable to model the effective behavior of the RUCs as linear elastic. For this purpose in Fig. 6, the distribution of maximum in-plane principal strain is shown. The maximum value is close to 4.5%, which is almost 30% less than the applied strain of 6.67%. Thus, in further investigations, we can assume that the maximum strains in the material are smaller than the strains applied on the structure, which can again be associated with predominant bending behavior of the shells. Figure 6 also shows the lattice structure in an experimental compression test for visual comparison.

Finally, a comprehensive comparison of experimental and simulation results of the compression of the shell lattices is performed for 6 different aspect ratios h/a, see Fig. 7. For each aspect ratio, three structures are MSLA 3D printed and subjected to compression testing. Thus, the averaged load–displacement curves of each three experiments are depicted in Fig. 7. The repetition of the experiment is carried out to ensure the reliability and accuracy of the experimental results. Up to an aspect ratio of $h/a = 0.20$, the experiments and the shell FEM are in very close agreement. However, for $h/a = 0.24$ and above, the simulations tend to underestimate the experimental results. The root of the error possible stems from the general restrictions of shell theories, which are only applicable for thin to moderately thick structures and tend to under-estimate the stiffness of a thicker, less shell-like structure.

Overall, the results presented show that the finite strain shell model can accurately, reliably and efficiently simulate

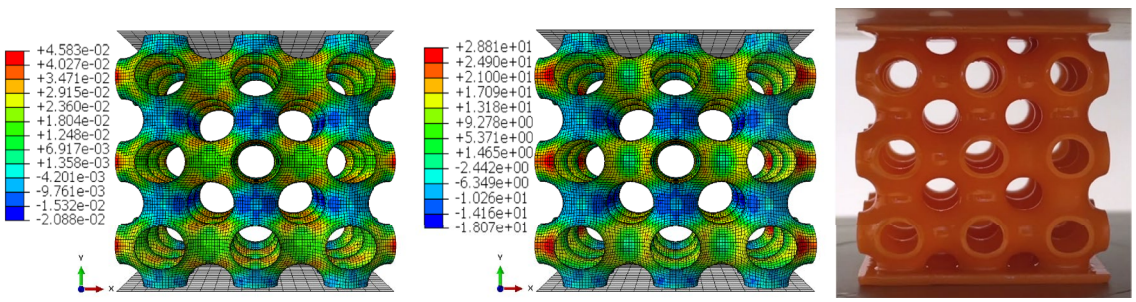

(a) FEM colored by max. in-plane strain (b) FEM colored by max. in-plane stress (c) Experimental compression test

Fig. 6 Illustration of compressed lattice structures in the finite element simulations and experiments

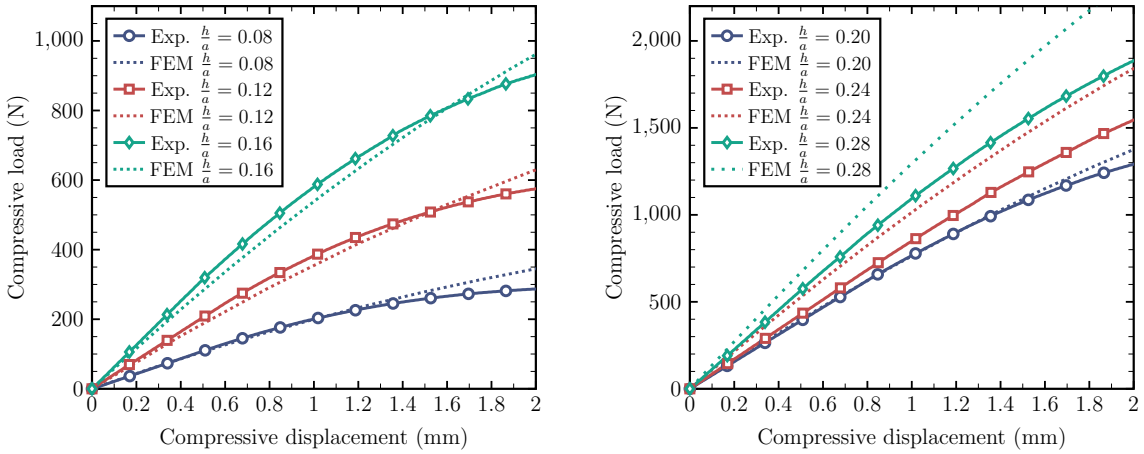

Fig. 7 Comparison of experimental and simulation load–displacement curves of compression tests of $3 \times 3 \times 3$ lattices with different aspect ratios h/a of the SP RUCs

Table 1 Mesh refinement convergence study of the stress value (MPa) for an SP RUC ($a = b = c = 5$ mm, $h/a = 0.20$) under various loading conditions applied using periodic boundary conditions

	Uniaxial σ_{11}		Equibiaxial $\sigma_{11} = \sigma_{22}$		Volumetric σ_{ii}		Simple shear σ_{12}	
No. of elements	$\epsilon = 3\%$	$\epsilon = -3\%$	$\epsilon = 3\%$	$\epsilon = -3\%$	$\epsilon = 3\%$	$\epsilon = -3\%$	$\epsilon = 3\%$	$\epsilon = -3\%$
208	2.1798	−1.9289	3.8273	−2.9845	5.7072	−3.7563	0.7263	−0.7261
784	2.1601	−1.8980	3.8024	−2.9450	5.6760	−3.7281	0.7165	−0.7166
1792	2.1552	−1.8942	3.7924	−2.9378	5.6641	−3.7207	0.7125	−0.7125
3236	2.1528	−1.8907	3.7906	−2.9339	5.6609	−3.7184	0.7123	−0.7123
9342	2.1520	−1.8900	3.7891	−2.9326	5.6589	−3.7172	0.7117	−0.7117

the mechanical behavior of additively manufactured SP TPMS structures.

3.2 Investigation of microscale behavior

Having a validated simulation model for SP shell lattices, this model is now investigated and verified in terms of its microscale behavior. For this purpose, we first study the required mesh refinement for accurately simulating an SP RUC with $a = b = c = 5$ mm using periodic boundary conditions and then confirm the independence of the homogenization results from the RVE size.

Table 1 presents the convergence of the normal or shear stress values for applied strains of $\epsilon = \pm 3\%$ for various applied deformation cases for an RUC with $h/a = 0.20$. The number of shell elements used in the calculation varies between 208 to 9342. The convergence of the four types of displacement loading, namely uniaxial, equibiaxial, volumetric, and simple shear, is examined under both tensile and compressive strain conditions. The rate of convergence is found to be fast and acceptable in all cases. The results obtained with 1792 elements are considered sufficiently accurate for further analysis. Furthermore, Fig. 8a shows the resulting load–displacement curves for strains ranging from – 6 to 6%. Within this strain range, it is observed that equibiaxial and volumetric compression states experience compressive instabilities, for which the nonlinear finite strain simulations do not converge anymore. On the other hand, the uniaxial and simple shear states exhibit a mostly linear behavior within this strain range.

To investigate the dependency of the homogenization procedure on the number of unit cells in the RVE, RVEs with $1 \times 1 \times 1$ (1^3), $2 \times 2 \times 2$ (2^3), and $3 \times 3 \times 3$ (3^3) RUCs with $a = b = c = 5$ mm and $h/a = 0.12$ are subjected to the aforementioned four strain conditions under PBC. In Fig. 8b, it can be seen that for all cases the results with different number of unit cells are in exact agreement. This is to be expected and confirms the correct implementation of the PBC and the homogenization procedure. However, it can be observed that the instabilities and termination of convergence occur at different compressive strains for the equibiaxial and volumetric cases. This is in fact also to be expected, since instabilities can be size-dependent and different buckling modes can be triggered for different RVE sizes. In such cases, effective, homogenized modeling of the microstructural behavior is not possible anymore, at least using the classical Cauchy continuum theory.

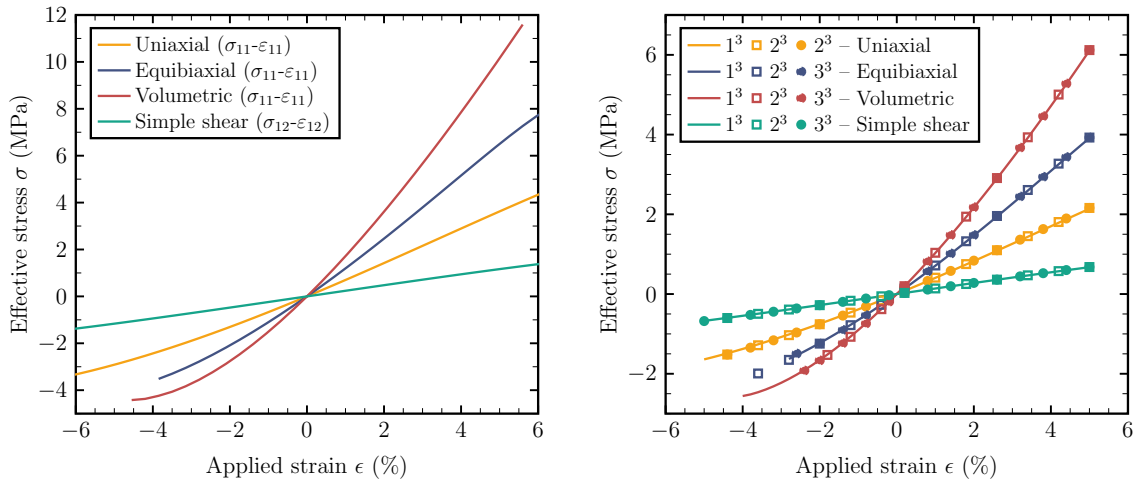

(a) Load-displacement curves for four different load cases of a RUC with $h/a = 0.20$

(b) Dependency of the homogenization results on the RVE size for a RUC with $h/a = 0.12$

Fig. 8 Microstructure homogenization of SP RVEs with $a = b = c = 5$ mm under periodic boundary conditions **a** for different applied deformation cases and **b** with different number of RUCs in the RVE

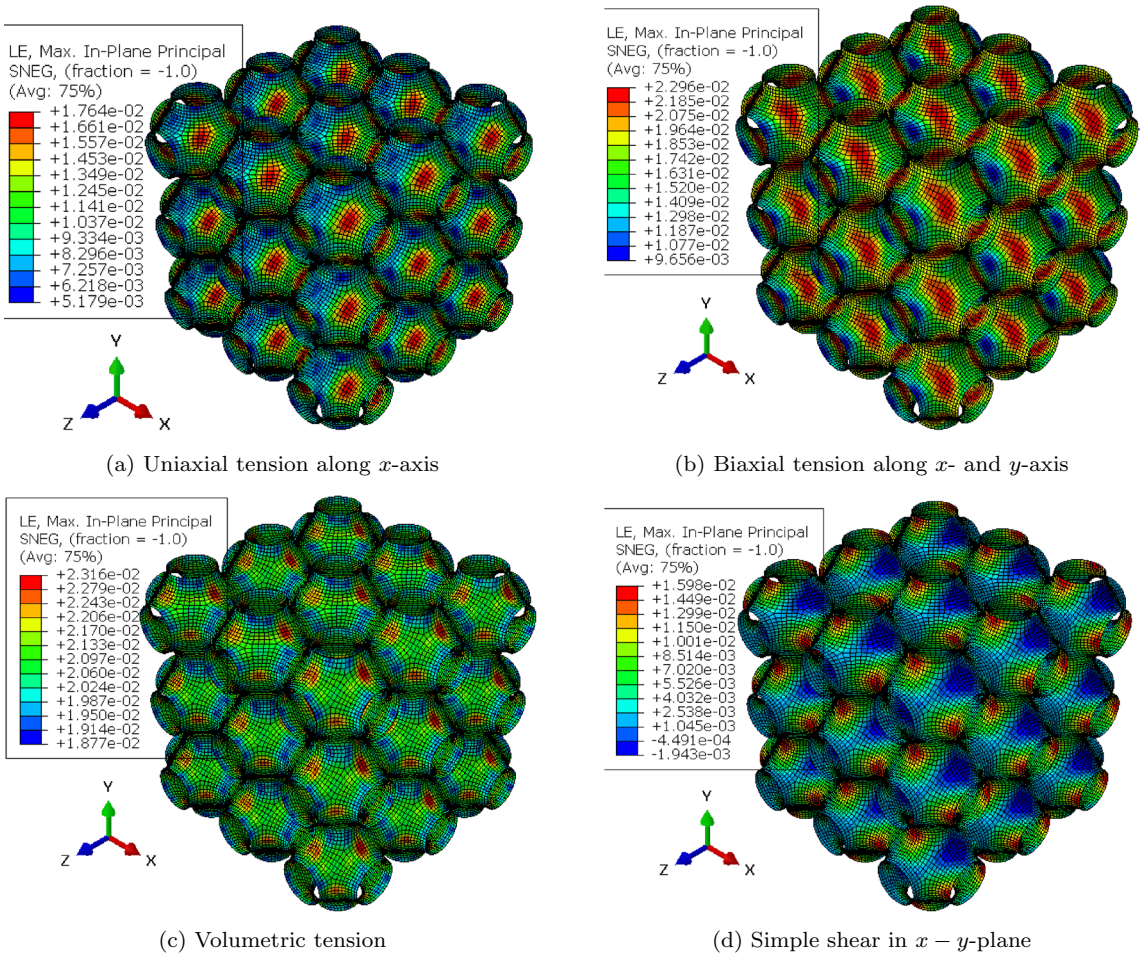

(a) Uniaxial tension along x-axis

(b) Biaxial tension along x- and y-axis

(c) Volumetric tension

(d) Simple shear in $x - y$-plane

Fig. 9 Maximum in-plane strain distributions of the $3 \times 3 \times 3$ RVE of SP RUCs with $a = b = c = 5$ mm and $h/a = 0.12$ under PBC at an applied tensile strain of 2%

Additionally, Fig. 9 shows the maximum in-plane principal strain distributions over the RVE with $3 \times 3 \times 3$ RUCs at the applied strain of 2%. It is apparent that the strain distributions are periodic for all four cases. Furthermore, it can be observed that the maximum strain values within the RUC are close to the applied strain, indicating that linearization can safely be employed.

Overall, it can be concluded that in the applied strain range of -2% to 4%, the effective behavior of the SP lattice can be safely approximated as linear elastic for all cases. Thus, this range is suitable for linear elastic multiscale analysis of functionally graded SP lattice structures. Note that these analyses have been carried out using the nonlinear shell formulation and hyperelastic constitutive model to safely determine this range without potentially neglecting crucial geometrical and material nonlinear effects.

3.3 Homogenization of parametric effective material model

After having verified the microscale simulation model, we proceed with the homogenization of an effective material model for the parametrized SP lattice. First, data in terms of parameter–elasticity tensor couples, compare Eq. (14), must be generated and then the physics-augmented FFNN can be fitted.

For the generation of the dataset $\mathcal{D}$, we vary the parameters a, b, c uniformly in $\{4.0, 4.5, \dots, 7.5\}$ mm and the shell thickness h in $\{0.4, 0.5, \dots, 1.4\}$ mm. These ranges are chosen in view of the manufacturability of the SP lattices using MSLA, as well as the validity of the shell theory. Overall, this yields $8^3 \cdot 11$ combinations and thus a dataset size $n = 5632$. For each parameter combination $\boldsymbol{t}_i$, the corresponding SP RUC geometry is created and meshed with 1792 shell elements. Then, 6 microscale simulations with PBCs are carried out to determine the effective elasticity tensor $\hat{\mathbb{C}}_i$, as discussed in Sect. 2.3.

The effect of the variation of geometric parameters within the dataset $\mathcal{D}$ on the effective, homogenized behavior of the Schwarz primitive is illustrated in Fig. 10a. SP RUCs with $a = 4, 5, 6, 7$ mm, $b = c = 5$ mm, and $h = 0.4, 0.5, \dots, 1.4$ mm are subject to uniaxial loading with 1% applied strain and periodic boundary conditions. Figure 10a shows the value of the homogenized stress σ_{11} over the thickness h for different values of a. The results indicate that by increasing the thickness, as can be expected, the effective stress increases for all choices of a. Furthermore, as the a increases, the difference in the effective stress decreases. Figure 10b visualizes the stress distributions for SP RUCs with $h = 1.2$ mm and $a = 4, 5, 6, 7$ mm. As can be seen, the pattern of the stress distributions and the position of maximum stress shift as the length of the RUC increases.

For the training of the neural network model to predict $\mathbb{C}(\boldsymbol{t})$, i.e., the optimization of its hyperparameters, the dataset $\mathcal{D}$ is randomly split into a calibration dataset $\mathcal{D}_c$ and an evaluation dataset $\mathcal{D}_e$. Here, we use 60 % of the overall dataset for $\mathcal{D}_c$. After calibrating the model on $\mathcal{D}_c$, it is evaluated on $\mathcal{D}_e$. Only when the accuracy of the predictions is equally good on $\mathcal{D}_c$ and $\mathcal{D}_e$, it can be assumed that the model is able to generalize, meaning that it can make reliable predictions for inputs not seen in the calibration process. Thus, the parameter optimization is initialized three times, where each time different random initial values for the model parameters are used, as well as new random splits of the dataset into calibration and evaluation sets. In this way,

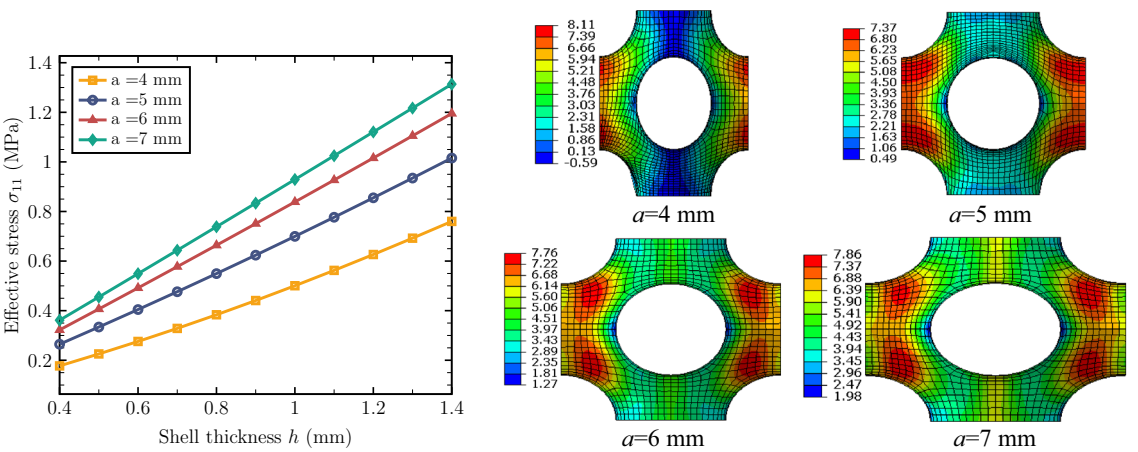

(a) Shell thickness h versus effective stress σ_{11}

(b) Distribution of stress $\sigma_{m,11}$ for RUCs with shell thickness $h = 1.2$ and $a = 4, 5, 6$, and 7 mm, respectively

Fig. 10 Illustration of the effect of the variation of the geometric parameters a and h on the effective stress of SP RUCs under uniaxial loading at 1% applied strain

Table 2 MSEs of the neural networks predictions of the effective constitutive tensors $\mathbb{C}(\boldsymbol{t})$ of the parameterized SP RUC on the different datasets for a different model calibration runs

calibration	$\log_{10}$(MSE) on...			
run	calibration $\mathcal{D}_c$	evaluation $\mathcal{D}_e$	case A	case B
1	2.39	2.40	2.34	2.41
2	−0.77	−0.76	−0.77	−0.78
3	−0.77	−0.80	−0.80	−0.85

different minima of the optimization problem can be found, out of which the best can be chosen for further evaluation.

The MSEs for the three different model calibrations are presented in Table 2 for the different datasets. While the first model calibration was stuck in a local minimum where $G_{11} = G_{21} = G_{31} \approx 0$ and thus shows a very high MSE, the other two model calibrations both show an excellent interpolation of the calibration data, meaning a low MSE value for the calibration dataset, and an excellent prediction on the evaluation dataset. In particular, the evaluation loss for model calibration 2 and 3 is approximately as high as the calibration loss.

In addition to $\mathcal{D}_c$ and $\mathcal{D}_e$, to visualize some model predictions, two variations of parameter combinations are generated, which are denoted as "case A"and "case B", see also Fig. 11. Also for these two datasets, which feature each 20 data points with smoothly progressing parameter values, which are mostly not part of $\mathcal{D}$, the MSEs shown in Table 2 are similar to the ones on $\mathcal{D}_c$ and $\mathcal{D}_e$. Thus, case A and case B are somewhat representative for the overall prediction quality of the model.

For the following investigations, the calibrated model of the third model calibration is chosen, as it performs the best on the evaluation dataset. In Fig. 11, the model predictions for case A and case B, as well as the corresponding coefficients of the effective elasticity tensors from the numerical homogenization are presented. Case A is symmetric in the parameter combination and the results show that the model learned also this underlying symmetry. In particular, in the middle the model learned to be cubic, meaning same parameter values. Case B features a somewhat arbitrary parameter variation and also shows an excellent prediction quality. Note the different orders of magnitude of the different components for some fixed parameter values, as well as the different orders of magnitude in the single components when changing the parameter values.

3.4 Multiscale simulation and verification

Finally, the homogenized effective material model can be applied for the multiscale simulation of 3D lattice structures consisting of (functionally graded) SP RUCs and be evaluated against direct full-scale simulations.

In the first case study, we consider a 3D solid lattice made of a uniform, homogeneous SP RUC geometry with $a = b = c = 5$ mm and $h = 1$ mm $(h/a = 0.20)$.

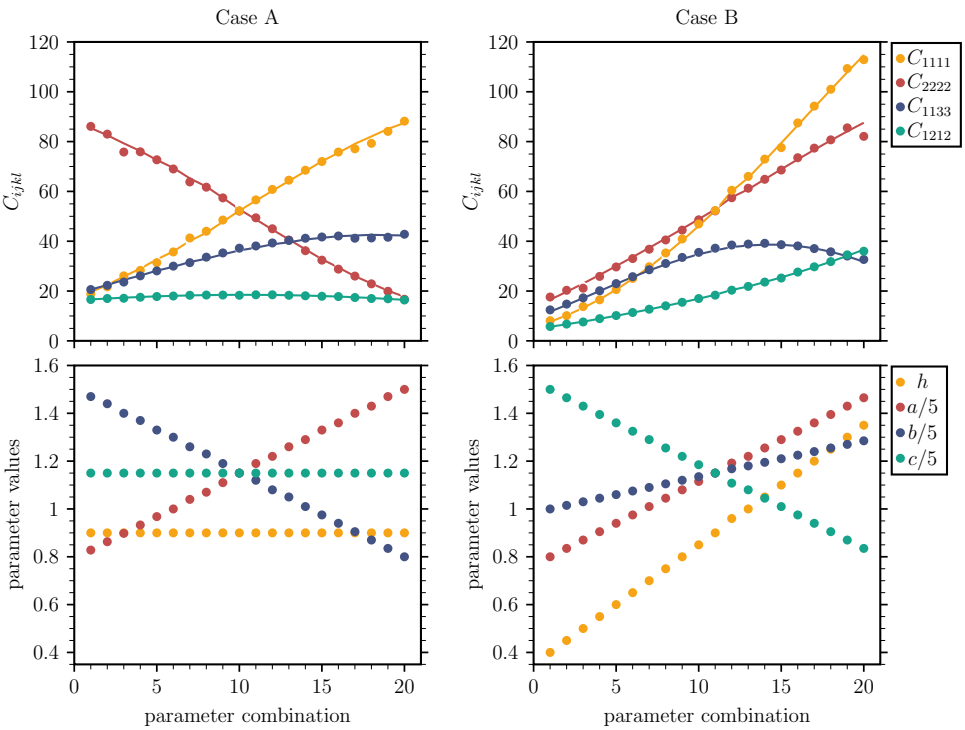

Fig. 11 Progression of the coefficients of the homogenized elasticity tensor $\mathbb{C}(\boldsymbol{t})$ (top row) for the two variations of continuous parameter combinations case A and case B (left and right). The parameter values $\boldsymbol{t}$ are provided in the bottom row. Dots denote the data, while continuous lines denote the neural network model predictions

The dimensions of the 3D solid are constant in the x- and y-directions, with $L_1 = 100$ mm and $L_2 = 100$ mm. However, we consider three different heights (in the z-direction), i.e., $L_3 = 50, 100, 150$ mm. Thus, the full-scale models consist of $10 \times 10 \times 5$, $10 \times 10 \times 10$, and $10 \times 10 \times 15$ RUCs, respectively. For the homogenized model, the corresponding effective material properties are obtained as: $C_{1111} = C_{2222} = C_{3333} = 68.711$ MPa, $C_{1122} = C_{1133} = C_{2233} = 46.39$ MPa, and $C_{1212} = C_{1313} = C_{2323} = 24.2$ MPa.

For a first investigation, the boundary conditions are described using the abbreviation C-C-C-C-F-L, where the four sides (left, right, front, and back) are clamped (C), the bottom surface is free (F), and the top surface is subject to a uniform pressure load (L) with value $p_0 = 0.5\,\text{N/mm}^2$.

Figure 12 shows the distribution of the z-displacement u_3 graphically for both the full-scale and the homogenized models simulated in Abaqus. The displacement distribution is very similar, indicating the reliability of the homogenized model. To show the accuracy, Fig. 3 compares the results obtained using the full-scale, direct shell simulation in Abaqus with the multiscale simulation using FEM in Abaqus and using DQM in an in-house code. The results converge rapidly and are generally in good agreement, which confirms the viability of the multiscale approach and verifies the DQM against Abaqus. Note that for FEM $N_x = N_y = N_z$ denotes the number of elements used in x, y, z-directions, while for the DQM it denotes the polynomial degree. The total number of degrees of freedom is however comparable for FEM and DQM with the same $N_x = N_y = N_z$. Furthermore, note that a perfect agreement of full-scale and multiscale simualtions is not to be expected, since boundary and size effects may have an influence.

For a second investigation of the same type of structure, we just change the boundary conditions to C-C-F-F-F-L, indicating that the left and right sides are clamped (C),

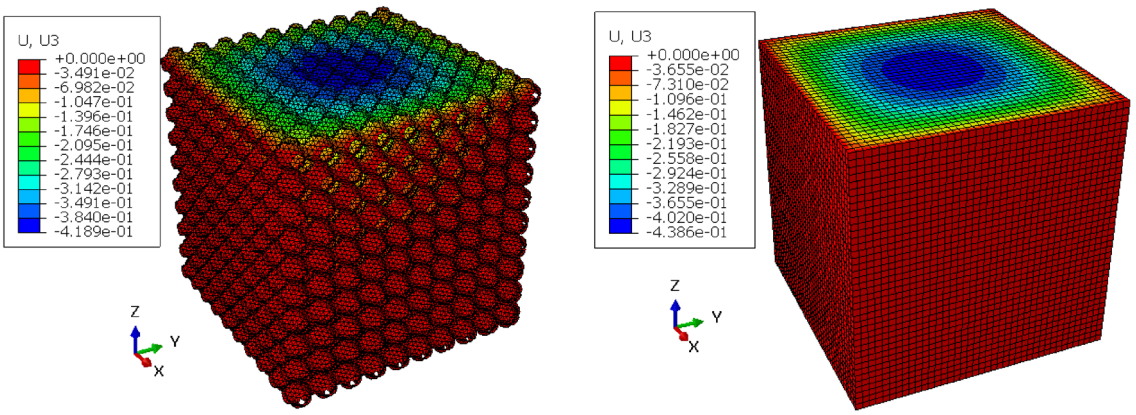

(a) Direct, full-scale simulation with $10 \times 10 \times 10$ RUCs

(b) Multiscale FEM simulation with effective material model

Fig. 12 Comparison of **a** full-scale and **b** multiscale simulation of a 3D lattice structure consisting of uniform SP RUCs with $a = b = c = 5$ mm and $h/a = 0.20$. C-C-C-C-F-L boundary conditions are applied and the displacement field u_3 is visualized

Table 3 Comparison of the maximum displacement u_3 (in mm) of 3D lattice structures consisting of uniform SP RUCs subject to C-C-C-C-F-L boundary conditions

	Lattice size	$10 \times 10 \times 5$	$10 \times 10 \times 10$	$10 \times 10 \times 15$
Full-scale shell model	-	0.5852	0.4189	0.4319
Multiscale (Abaqus)	$N_x = N_y = N_z$			
	10	0.5768	0.4638	0.4600
	20	0.5699	0.4402	0.4340
	33	0.5731	0.4386	0.4348
	50	0.5741	0.4393	0.4352
Multiscale (DQM)	$N_x = N_y = N_z$			
	9	0.5698	0.4257	0.4380
	13	0.5689	0.4312	0.4353
	17	0.5689	0.4374	0.4340
	21	0.5690	0.4373	0.4335
	25	0.5691	0.4372	0.4333

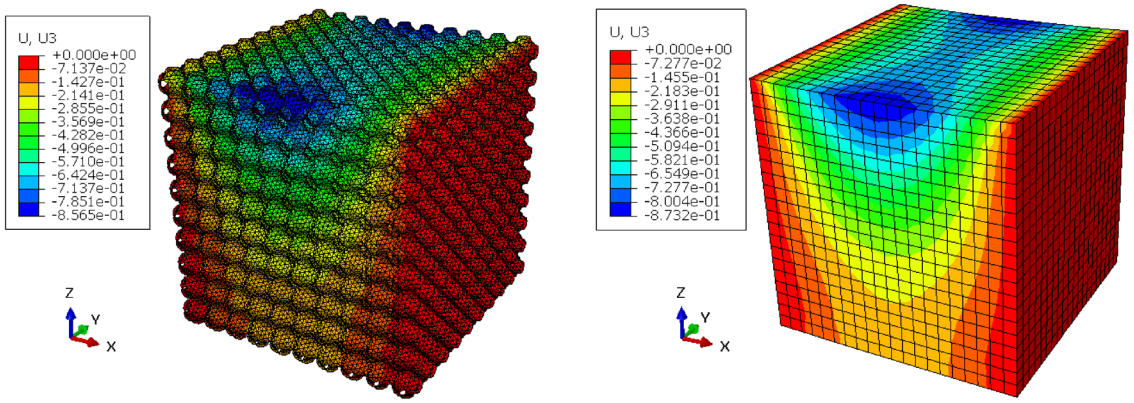

(a) Direct, full-scale simulation with $10 \times 10 \times 10$ RUCs

(b) Multiscale FEM simulation with effective material model

Fig. 13 Comparison of **a** full-scale and **b** multiscale simulation of a 3D lattice structure consisting of uniform SP RUCs with $a = b = c = 5$ mm and $h/a = 0.20$. C-C-F-F-F-L boundary conditions are applied and the displacement field u_3 is visualized

Table 4 Comparison of the maximum displacement u_3 (in mm) of 3D lattice structures consisting of uniform SP RUCs subject to C-C-F-F-F-L boundary conditions

	Lattice size	$10 \times 10 \times 5$	$10 \times 10 \times 10$	$10 \times 10 \times 15$
Full-scale shell model	-	1.364	0.8565	0.8793
Multiscale (Abaqus)	$N_x = N_y = N_z$			
	10	1.2677	0.8863	0.8669
	20	1.2773	0.8732	0.8530
	33	1.2854	0.8755	0.8550
	50	1.2878	0.8762	0.8555
Multiscale (DQM)	$N_x = N_y = N_z$			
	9	1.2713	0.8730	0.8547
	13	1.2765	0.8711	0.8504
	17	1.2771	0.8710	0.8496
	21	1.2771	0.8709	0.8493
	25	1.2771	0.8709	0.8493

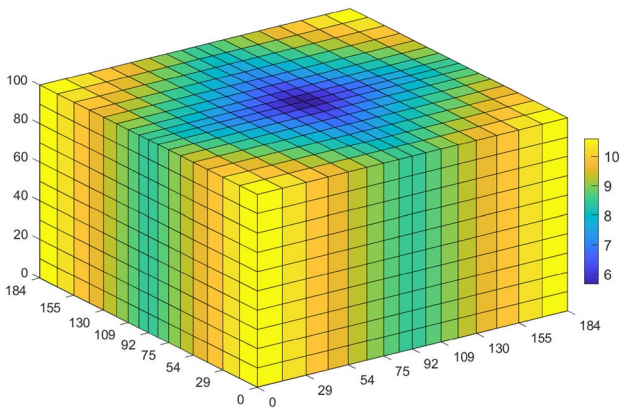

Fig. 14 Illustration of geometric parameter distribution of the functionally graded 3D lattice. Colors indicate $\sqrt{a^2 + b^2}$ of the unit cells

while the front, back, and bottom surfaces are free (F), and the top surface is subject to a uniform pressure load (L) with $p_0 = 0.5\,\text{N/mm}^2$. The accuracy and convergence of the results for these different boundary and loading conditions can be assessed in Figs. 13 and 4. Once again, a good visual agreement of the displacement u_3 obtained from full-scale and multiscale FEM simulation can be observed in Figs. 13 and 4 shows good convergence behavior as well as a good agreement of maximum u_3 for all 3 approaches.

Finally, a functionally graded lattice structure with a non-uniform distribution of the geometric parameters of the SP RUCs is investigated, see Figs. 2d and 14. The dimensions of the 3D structure are $L_1 = L_2 = 184$ mm and the height is varied as either $L_3 = 100$ mm or $L_3 = 150$ mm. The full-scale model consists of 16 non-uniform RUCs in the x- and y-directions, with graded sizes ranging from 15 to 8 mm, i.e., with $a = b \in \{7.5, \ldots, 4.5, 4.0, 4.0, 4.5, \ldots, 7.5\}$ mm. All unit cells have a height of 10 mm in the z-direction and, i.e., $c = 5$ mm, and a uniform thickness of $h = 1$ mm. The

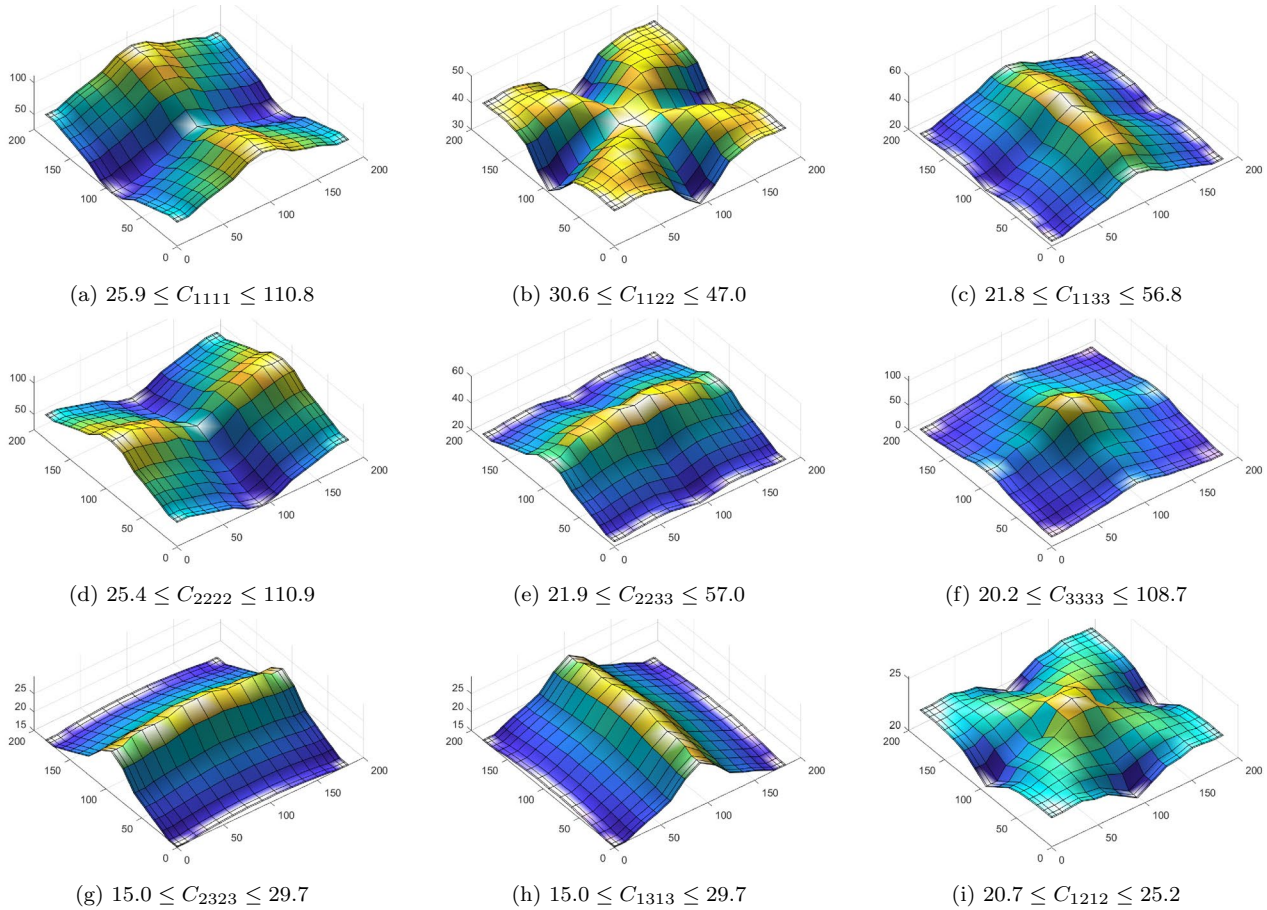

(a) $25.9 \leq C_{1111} \leq 110.8$ (b) $30.6 \leq C_{1122} \leq 47.0$ (c) $21.8 \leq C_{1133} \leq 56.8$

(d) $25.4 \leq C_{2222} \leq 110.9$ (e) $21.9 \leq C_{2233} \leq 57.0$ (f) $20.2 \leq C_{3333} \leq 108.7$

(g) $15.0 \leq C_{2323} \leq 29.7$ (h) $15.0 \leq C_{1313} \leq 29.7$ (i) $20.7 \leq C_{1212} \leq 25.2$

Fig. 15 Distribution of the resulting coefficients of the effective material model of the functionally graded lattice structure with dimensions 184 mm×184 mm in the $x-y$-plane. The values of C_{ijkl} are given in MPa

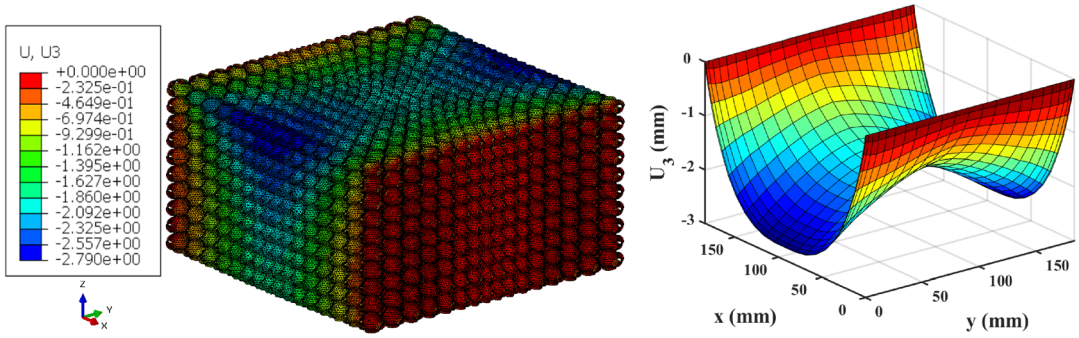

(a) Direct, full-scale simulation with $16 \times 16 \times 10$ RUCs (b) Displacement on top surface of multiscale DQM

Fig. 16 Comparison of **a** full-scale and **b** multiscale DQM simulation of a functionally graded 3D lattice structure consisting of non-uniform SP RUCs. C-C-F-F-F-L boundary conditions are applied and the displacement field u_3 is visualized. Note that for the DQM method, only the result on the top surface is visualized

distributions of the geometric parameters of the functionally graded SP lattice are visualized in Fig. 14. Furthermore, the material coefficients obtained from the neural network model, which are used in the multiscale DQM and result from the functional grading in the $x-y$-plane, are illustrated in Fig. 15. Again, the boundary conditions are C-C-F-F-F-L

Table 5 Comparison of the maximum displacement u_3 (in mm) of functionally graded 3D lattice structures consisting of non-uniform SP RUCs subject to C-C-F-F-F-L boundary conditions

	Lattice size	$16 \times 16 \times 10$	$16 \times 16 \times 15$
Full-scale shell model		2.790	2.362
Multiscale (DQM)	$N_x = N_y = N_z$		
	9	2.8600	2.3315
	13	2.8434	2.3146
	17	2.8410	2.3174
	19	2.8294	2.3073
	21	2.8383	2.3120

with the uniform pressure load $p_0 = 0.5\ \mathrm{N/mm^2}$ on the top surface.

The deformation of the lattice structure with $16 \times 16 \times 10$ RUCs resulting from the full-scale shell simulation in Abaqus and the displacement distribution on the top surface resulting from the multiscale simulation of the 3D solid calculated using the differential quadrature method and the FFNN material model are shown in Fig. 16. Visually, the results are in good agreement, as the magnitudes and patterns of the z-displacement u_3 are similar. Note that here solely the DQM is used for the multiscale analysis, since such a grading of material parameters is difficult to realize in Abaqus.

Furthermore, Fig. 5 shows a comparison of the maximum z-displacement of the full-scale simulation with the DQM multiscale results for $16 \times 16 \times 10$ and $16 \times 16 \times 15$ RUCs. In both cases, the values of the max. u_3 are in good agreement and also the convergence behavior of the DQM for increasing the polynomial order N_i in all directions can be observed.

4 Conclusion

In this work, a computational framework for the multiscale modeling of functionally graded shell lattice structures is presented. The systematic procedure combines experiments and simulation at microscale, full-scale, and macroscale levels for the validation and detailed verifications of the numerical models and comparison studies.

Functional grading of microstructures can be realized through additive manufacturing, which is here exemplified using masked stereolithography of a photopolymer material. Thus, the material behavior of the 3D printed polymer is first characterized for the validation of the full-scale simulation, in which Schwarz primitive TPMS structures are modeled by shell finite elements. The good agreement between the experimental and simulation results validates the accuracy and reliability of the simulation model. This shell model is then also employed for the microstructural homogenization of SP unit cells, which are parameterized by their geometric dimensions and shell thickness. The effective linear elastic material behavior of these metamaterials is represented by a physics-augmented neural network, which preserves the rhombic material symmetry and the positive definiteness of the parameterized elasticity tensors. It is demonstrated that this machine learning based approach can accurately express the homogenized material response of the SP RUCs. Finally, the multiscale simulation framework is completed by using the homogenized material model in FEM and DQM simulations of 3D solids. These macroscale simulations are verified against full-scale simulations using the shell model and a good agreement of multiscale with full-scale results, as well as proper convergence behavior of the full-scale simulations are observed. Furthermore, a functionally graded Schwarz primitive lattice structure is analyzed by combining the DQM with the ANN material model, which is also in good agreement with full-scale simulations.

Overall, we believe that this systematic and validated multiscale simulation framework can yield valuable insights for the design and additive manufacturing of functionally graded shell lattice structures. It was here demonstrated in application to MSLA 3D printing and the Schwarz primitive TPMS, but could likewise be applied to any other type of (additive) manufacturing method or microstructure type. In future work, we would like to include even further design parameters into the microscale homogenization procedure and the effective physics-augmented neural network material model, such as process parameters of the manufacturing method. Furthermore, since functionally graded lattice structures offer great potential in particular for energy absorption applications, we want to include dynamic and inelastic material behaviors, i.e., elasto-visco-plasticity with fracture or failure, into the microscale and effective material models.

Acknowledgements D.K.K. and O.W. acknowledge the support by the Deutsche Forschungsgemeinschaft (DFG—German Research Foundation)—Grant No. 492770117 and the Graduate School of Computational Engineering within the Centre of Computational Engineering at TU Darmstadt.

Funding Open Access funding enabled and organized by Projekt DEAL.

Declarations

Conflict of interest The authors have no competing interests to declare that are relevant to the content of this article.

References

1. Greer JR, Deshpande VS (2019) Three-dimensional architected materials and structures: Design, fabrication, and mechanical behavior. MRS Bull 44(10):750–757. https://doi.org/10.1557/mrs.2019.232
2. A. J. D. Shaikeea, H. Cui, M. O'Masta, X. R. Zheng, V. S. Deshpande, The toughness of mechanical metamaterials, Nature Materials https://doi.org/10.1038/s41563-021-01182-1
3. Zadpoor AA, Mirzaali MJ, Valdevit L, Hopkins JB (2023) Design, material, function, and fabrication of metamaterials. APL Mater 11(2):020401. https://doi.org/10.1063/5.0144454
4. Wang Y, Zhang L, Daynes S, Zhang H, Feih S, Wang MY (2018) Design of graded lattice structure with optimized mesostructures for additive manufacturing. Mater Des 142:114–123. https://doi.org/10.1016/j.matdes.2018.01.011
5. Veloso F, Gomes-Fonseca J, Morais P, Correia-Pinto J, Pinho AC, Vilaça JL (2022) Overview of methods and software for the design of functionally graded lattice structures. Adv Eng Mater 24(11):2200483. https://doi.org/10.1002/adem.202200483
6. Choy SY, Sun C-N, Leong KF, Wei J (2017) Compressive properties of functionally graded lattice structures manufactured by selective laser melting. Mater Des 131:112–120. https://doi.org/10.1016/j.matdes.2017.06.006
7. Bai L, Gong C, Chen X, Sun Y, Xin L, Pu H, Peng Y, Luo J (2020) Mechanical properties and energy absorption capabilities of functionally graded lattice structures: Experiments and simulations. Int J Mech Sci 182:105735. https://doi.org/10.1016/j.ijmecsci.2020.105735
8. Weeger O, Kang Y, Yeung S-K, Dunn M (2016) Optimal design and manufacture of active rod structures with spatially variable materials, 3D Printing and Additive Manufacturing 3(4):204–215. https://doi.org/10.1089/3dp.2016.0039
9. Valizadeh I, Al boud A, Dörsam E, Weeger O (2021) Tailoring of functionally graded hyperelastic materials via grayscale mask stereolithography 3d printing. Addit Manuf 47:102108. https://doi.org/10.1016/j.addma.2021.102108
10. Valizadeh I, Weeger O (2022) Parametric visco-hyperelastic constitutive modeling of functionally graded 3d printed polymers. Int J Mech Sci 226:107335. https://doi.org/10.1016/j.ijmecsci.2022.107335
11. Kim TY, Park S-H, Park K (2021) Development of functionally graded metamaterial using selective polymerization via digital light processing additive manufacturing. Addit Manuf 47:102254. https://doi.org/10.1016/j.addma.2021.102254
12. Kumar S, Tan S, Zheng L, Kochmann DM (2020) Inverse-designed spinodoid metamaterials. npj Computational Materials 6(1):1–10. https://doi.org/10.1038/s41524-020-0341-6
13. Han L, Che S (2018) An overview of materials with triply periodic minimal surfaces and related geometry: From biological structures to self-assembled systems. Adv Mater 30(17):1705708. https://doi.org/10.1002/adma.201705708
14. Mackay AL (1985) Periodic minimal surfaces. Nature 314(6012):604–606. https://doi.org/10.1038/314604a0
15. Zhang L, Feih S, Daynes S, Chang S, Wang MY, Wei J, Lu WF (2018) Energy absorption characteristics of metallic triply periodic minimal surface sheet structures under compressive loading. Addit Manuf 23:505–515. https://doi.org/10.1016/j.addma.2018.08.007
16. Bonatti C, Mohr D (2019) Mechanical performance of additively-manufactured anisotropic and isotropic smooth shell-lattice materials: Simulations and experiments. J Mech Phys Solids 122:1–26. https://doi.org/10.1016/j.jmps.2018.08.022
17. Guo X, Ding J, Li X, Qu S, Song X, Fuh JYH, Lu WF, Zhai W (2022) Enhancement in the mechanical behaviour of a Schwarz primitive periodic minimal surface lattice structure design. Int J Mech Sci 216:106977. https://doi.org/10.1016/j.ijmecsci.2021.106977
18. Feng J, Fu J, Yao X, He Y (2022) Triply periodic minimal surface (TPMS) porous structures: From multi-scale design, precise additive manufacturing to multidisciplinary applications. International Journal of Extreme Manufacturing 4(2):022001. https://doi.org/10.1088/2631-7990/ac5be6
19. Plocher J, Panesar A (2020) Effect of density and unit cell size grading on the stiffness and energy absorption of short fibre-reinforced functionally graded lattice structures. Addit Manuf 33:101171. https://doi.org/10.1016/j.addma.2020.101171
20. N. Sathishkumar, N. Arunkumar, S. V. Rohith, R. R. Hariharan, Effect of varying unit cell size on energy absorption behaviour of additive manufactured TPMS PETG lattice structure, Progress in Additive Manufacturing https://doi.org/10.1007/s40964-023-00407-w
21. Roudbarian N, Jebellat E, Famouri S, Baniasadi M, Hedayati R, Baghani M (2022) Shape-memory polymer metamaterials based on triply periodic minimal surfaces. Eur J Mech A Solids 96:104676. https://doi.org/10.1016/j.euromechsol.2022.104676
22. Kochmann DM, Hopkins JB, Valdevit L (2019) Multiscale modeling and optimization of the mechanics of hierarchical metamaterials. MRS Bull 44(10):773–781. https://doi.org/10.1557/mrs.2019.228
23. Abueidda DW, Abu Al-Rub RK, Dalaq AS, Lee D-W, Khan KA, Jasiuk I (2016) Effective conductivities and elastic moduli of novel foams with triply periodic minimal surfaces. Mech Mater 95(Supplement C):102–115. https://doi.org/10.1016/j.mechmat.2016.01.004
24. Feng J, Liu B, Lin Z, Fu J (2021) Isotropic porous structure design methods based on triply periodic minimal surfaces. Materials & Design 210:110050. https://doi.org/10.1016/j.matdes.2021.110050
25. Valizadeh I, Weeger O (2020) Nonlinear multiscale simulation of instabilities due to growth of an elastic film on a microstructured substrate. Arch Appl Mech 90(11):2397–2412. https://doi.org/10.1007/s00419-020-01728-w
26. N. Kladovasilakis, K. Tsongas, I. Kostavelis, D. Tzovaras, D. Tzetzis, Effective mechanical properties of additive manufactured triply periodic minimal surfaces: Experimental and finite element study, The International Journal of Advanced Manufacturing Technology https://doi.org/10.1007/s00170-022-09651-w
27. A. M. Abou-Ali, O. Al-Ketan, D.-W. Lee, R. Rowshan, R. K. Abu Al-Rub, Mechanical behavior of polymeric selective laser sintered ligament and sheet based lattices of triply periodic minimal surface architectures, Materials and Design 196 (2020) 109100. https://doi.org/10.1016/j.matdes.2020.109100
28. Günther F, Hirsch F, Pilz S, Wagner M, Gebert A, Kästner M, Zimmermann M (2022) Structure-property relationships of imperfect additively manufactured lattices based on triply periodic minimal surfaces. Mater Des 222:111036. https://doi.org/10.1016/j.matdes.2022.111036

29. Jiang W, Liao W, Liu T, Shi X, Wang C, Qi J, Chen Y, Wang Z, Zhang C (2021) A voxel-based method of multiscale mechanical property optimization for the design of graded TPMS structures. Mater Des 204:109655. https://doi.org/10.1016/j.matdes.2021.109655
30. G. C. Y. Peng, M. Alber, A. Buganza Tepole, W. R. Cannon, S. De, S. Dura-Bernal, K. Garikipati, G. Karniadakis, W. W. Lytton, P. Perdikaris, L. Petzold, E. Kuhl, Multiscale modeling meets machine learning: What can we learn?, Archives of Computational Methods in Engineering https://doi.org/10.1007/s11831-020-09405-5
31. Aggarwal CC (2018) Neural Networks and Deep Learning, 1st edn. Springer, New York
32. S. Kollmannsberger, D. D'Angella, M. Jokeit, L. Herrmann, Deep Learning in Computational Mechanics, Vol. 977 of Studies in Computational Intelligence, Springer, 2021. https://doi.org/10.1007/978-3-030-76587-3
33. Hornik K (1991) Approximation capabilities of multilayer feedforward networks. Neural Netw 4(2):251–257. https://doi.org/10.1016/0893-6080(91)90009-T
34. Xu K, Huang DZ, Darve E (2021) Learning constitutive relations using symmetric positive definite neural networks. J Comput Phys 428:110072. https://doi.org/10.1016/j.jcp.2020.110072
35. C. F. Jekel, K. E. Swartz, D. A. White, D. A. Tortorelli, S. E. Watts, Neural network layers for prediction of positive definite elastic stiffness tensors, Pre-print under review arXiv:2203.13938
36. Klein DK, Fernández M, Martin RJ, Neff P, Weeger O (2022) Polyconvex anisotropic hyperelasticity with neural networks. J Mech Phys Solids 159:104703. https://doi.org/10.1016/j.jmps.2021.104703
37. Klein DK, Ortigosa R, Martínez-Frutos J, Weeger O (2022) Finite electro-elasticity with physics-augmented neural networks. Comput Methods Appl Mech Eng 400:115501. https://doi.org/10.1016/j.cma.2022.115501
38. L. Linden, D. K. Klein, K. A. Kalina, J. Brummund, O. Weeger, M. Kästner, Neural networks meet hyperelasticity: A guide to enforcing physics, Pre-print under review arXiv:2302.02403
39. As'ad F, Avery P, Farhat C (2022) A mechanics-informed artificial neural network approach in data-driven constitutive modeling. Int J Numer Meth Eng 123(12):2738–2759. https://doi.org/10.1002/nme.6957
40. Vlassis NN, Sun W (2021) Sobolev training of thermodynamic-informed neural networks for interpretable elasto-plasticity models with level set hardening. Comput Methods Appl Mech Eng 377:113695. https://doi.org/10.1016/j.cma.2021.113695
41. Masi F, Stefanou I (2022) Multiscale modeling of inelastic materials with thermodynamics-based artificial neural networks (TANN). Comput Methods Appl Mech Eng 398:115190. https://doi.org/10.1016/j.cma.2022.115190
42. Thakolkaran P, Joshi A, Zheng Y, Flaschel M, De Lorenzis L, Kumar S (2022) NN-EUCLID: Deep-learning hyperelasticity without stress data. J Mech Phys Solids 169:105076. https://doi.org/10.1016/j.jmps.2022.105076
43. Z. Liu, Y. Du, Y. Chen, M. Tegmark, Physics-augmented learning: A new paradigm beyond physics-informed learning, 2021. arXiv:2109.13901
44. J. Mianroodi, S. Rezaei, N. Siboni, B.-X. Xu, D. Raabe, Lossless multi-scale constitutive elastic relations with artificial intelligence, npj Computational Materials 8 (2022) 67. https://doi.org/10.1038/s41524-022-00753-3
45. Eidel B (2023) Deep CNNs as universal predictors of elasticity tensors in homogenization. Comput Methods Appl Mech Eng 403:115741. https://doi.org/10.1016/j.cma.2022.115741
46. Fernández M, Fritzen F, Weeger O (2022) Material modeling for parametric, anisotropic finite strain hyperelasticity based on machine learning with application in optimization of metamaterials. Int J Numer Meth Eng 123(2):577–609. https://doi.org/10.1002/nme.6869
47. T. Gärtner, M. Fernández, O. Weeger, Nonlinear multiscale simulation of elastic beam lattices with anisotropic homogenized constitutive models based on artificial neural networks, Computational Mechanics 68. https://doi.org/10.1007/s00466-021-02061-x
48. Dassault Systemes SIMULIA Corp., ABAQUS/CAE 2021: SIMULIA User Assistance (2021)
49. Holzapfel GA (2000) Nonlinear Solid Mechanics: A Continuum Approach for Engineering, 2nd edn. Wiley, Amsterdam
50. Zohdi TI, Wriggers P (2005) An Introduction to Computational Micromechanics, Lecture Notes in Applied and Computational Mechanics, Springer-Verlag. Berlin Heidelberg. https://doi.org/10.1007/978-3-540-32360-0
51. Bargmann S, Klusemann B, Markmann J, Schnabel JE, Schneider K, Soyarslan C, Wilmers J (2018) Generation of 3d representative volume elements for heterogeneous materials: A review. Prog Mater Sci 96:322–384. https://doi.org/10.1016/j.pmatsci.2018.02.003
52. V. Ebbing, Design of Polyconvex Energy Functions for All Anisotropy Classes, Ph.D. thesis, Universität Duisburg-Essen (2010)
53. Haupt P (2002) Continuum Mechanics and Theory of Materials, 2nd edn. Springer, Berlin Heidelberg
54. Malekzadeh P (2009) Three-dimensional free vibration analysis of thick functionally graded plates on elastic foundations. Compos Struct 89(3):367–373. https://doi.org/10.1016/j.compstruct.2008.08.007
55. Setoodeh A, Shojaee M (2016) Application of TW-DQ method to nonlinear free vibration analysis of FG carbon nanotube-reinforced composite quadrilateral plates. Thin-Walled Structures 108:1–11. https://doi.org/10.1016/j.tws.2016.07.019
56. Jrad H, Mars J, Wali M, Dammak F (2018) Geometrically nonlinear analysis of elastoplastic behavior of functionally graded shells. Engineering with Computers 35(3):833–847. https://doi.org/10.1007/s00366-018-0633-3
57. Horn R, Johnson C (2013) Matrix Analysis, 2nd edn. Cambridge University Press, USA
58. K. A. Kalina, L. Linden, J. Brummund, M. Kästner, FEANN – An efficient data-driven multiscale approach based on physics-constrained neural networks and automated data mining arXiv:1048550/arXiv.2207.01045